



Doping engineering of carrier transporting layers for ambient-air-stable lead-free rudorffite solar cells prepared by thermal-assisted doctor blade coating

Kai-Chi Hsiao^a, Yen-Fu Yu^a, Ching-Mei Ho^a, Meng-Huan Jao^b, Yu-Hsiang Chang^a, Shih-Hsuan Chen^a, Yin-Hsuan Chang^a, Wei-Fang Su^{d,e}, Kun-Mu Lee^{a,b,c,*}, Ming-Chung Wu^{a,b,c,*}

^a Department of Chemical and Materials Engineering, College of Engineering, Chang Gung University, Taoyuan 33302, Taiwan

^b Green Technology Research Center, Chang Gung University, Taoyuan 33302, Taiwan

^c Division of Neonatology, Department of Pediatrics, Chang Gung Memorial Hospital at Linkou, Taoyuan 33305, Taiwan

^d Department of Materials Science and Engineering, National Taiwan University, Taipei 10617, Taiwan

^e Department of Materials Engineering, Ming Chi University of Technology, New Taipei City 24301, Taiwan

ARTICLE INFO

Keywords:

Rudorffite
Solar cell
Silver bismuth iodide
Lead-free
Blade coat
Stability

ABSTRACT

Nowadays, high-efficiency perovskite solar cells mainly comprise a lead-based light-absorber layer. Without a doubt, the unprecedented power conversion efficiency (PCE) of perovskite solar cells makes them an optimistic solution for sustainable or renewable energy sources. However, the toxic composition of lead, a notorious element for organisms, in perovskite solar cells and its stability in an ambient environment raise public concern. Therefore, resolving these two issues is urgent for developing perovskite solar cells. In this study, Ag₃BiI₆ rudorffite was selected as an active layer prepared by the thermal-assisted doctor blade coating method to replace the conventional lead-based perovskite active layer. To align the energy level between carrier transporting layers and the Ag₃BiI₆ light absorber layer, doping both carrier transporting layers improved the PCE of doctor-bladed devices from 2.06% to 2.77%. These devices can maintain 90% of their initial PCE after storing them unencapsulated in an ambient environment for over 3,000 h. This study also demonstrates a large 1.00 cm² device with a PCE of 2.03%. The lead-free, air-stable, and mass production processible properties make it a promising selection for photovoltaic materials.

1. Introduction

Organometal-halide perovskite materials (OMHP) have attracted lots of attention since they first emerged in 2009 [1]. Their outstanding optoelectronic properties, including direction bandgap, weak carrier binding energy at room temperature [2], long carrier diffusion length [3,4], and high absorption coefficient [5], have helped their photovoltaic performance climb to an unprecedented power conversion efficiency (PCE) of 25.7% in 2022 [6]. From a macroscopic point of view, the properties of OMHPs mainly depend on constructed components, such as A-site cation of methylammonium, formamidium, and cesium, B-site cation of lead and tin, and X-site anion of halide. Whereas, the chemical bonding between the constructed elements plays an influential role in exhibiting extraordinary optoelectronic properties. Typically, the

valence band maximum (VBM) of OMHP is mainly composed of anti-bonding hybridization of the *ns* orbital from B-site cations and the *np* orbital from X-site anions [7]. Due to the antibonding from hybridization of the *ns* and the *np* orbital, defects in OMHPs are restrained to shallow states closely located at the band edge rather than forming deep states in-between the energy bandgaps of OMHPs [8]. On the other hand, the high ionicity of bonding in OMHPs makes them feasible to construct high crystallinity even though the process is carried out at moderate temperature. The unique properties of relatively high defect tolerance and process flexibility allow OMHPs to be fabricated through the solution process.

However, the potential leakage of lead, a notorious element for organisms, from OMHPs photovoltaics has become a noticeable concern when such potential photovoltaics are rapidly developed and possibly

* Corresponding authors at: Department of Chemical and Materials Engineering, College of Engineering, Chang Gung University, Taoyuan 33302, Taiwan.
E-mail addresses: kmlee@cgu.edu.tw (K.-M. Lee), mingchungwu@cgu.edu.tw (M.-C. Wu).

<https://doi.org/10.1016/j.cej.2022.138807>

Received 1 June 2022; Received in revised form 19 July 2022; Accepted 23 August 2022

Available online 28 August 2022

1385-8947/© 2022 Elsevier B.V. All rights reserved.

integrated into our daily lives [9,10]. Many efforts have been devoted to searching for an alternative candidate to replace the toxic element lead in OMHP photovoltaics while retaining their photovoltaic performance. First, replacing lead with an element holding similar chemical properties is a straightforward methodology for lead reduction. In the same group as lead, tin shares similar physical and chemical properties with lead and becomes the first candidate to substitute lead in OMHP. The promising photovoltaic performance harvested from the lead-free light-absorber layer of methylammonium tin trihalide has reached 5.73% [11]. Yet, the photo-active tin-based OMHPs are only present at the metastable phase of perovskite constructed with the B-site cation of Sn^{2+} . With the external interference of oxygen or moisture, the Sn^{2+} tends to oxidize and form a photo-inactive phase of tin-based perovskite with the B-site cation of Sn^{4+} [12–14]. In addition, the influences of Sn, sharing similar chemical properties with lead, on human health are still unclear.

Alternatively, bismuth has been known to act as a non-toxic additive and be widely used in other organic reactions [15]. Also, bismuth with a similar electronic configuration of lead, which exhibits vacant $6p$ orbitals, allows it to construct a similar energy structure as a substitution for lead. The relatively stable oxidation state of bismuth compared with tin soon caught the attention of the photovoltaic research community for lead replacement [16–19]. The difference in valence electron configuration between group VA and group IVA allows bismuth substitution to induce a perovskite-derivative crystal structure, classified based on the formula of A_2AgBiX_6 and $\text{Ag}_a\text{Bi}_b\text{X}_{a+3b}$, where A is a monovalent cation of methylammonium, formamidium, cesium, or rubidium, and X is a halide anion [20–22]. The former is known as a double perovskite, and the latter is a rudorffite structure. A double perovskite photovoltaic of $\text{Cs}_2\text{AgBiBr}_6$ film with high film quality was prepared through a single-crystal $\text{Cs}_2\text{AgBiBr}_6$ solution and demonstrated a PCE of 1.22% [23]. Through a systematic study of the annealing effect on crystallinity and photovoltaic properties by low pressure-assisted method, the PCE of double perovskite photovoltaic can be improved to 1.44% with environmentally stable power output [24]. Although double perovskite inherits similarities with OMHPs, their wide bandgap with indirect band structure and inferior carrier transportation result in a mediocre PCE when serving as a light absorber layer [15,23,24]. On the other hand, rudorffites, namely silver bismuth iodide (SBI), exhibit a direct band structure with a bandgap lower than 2.0 eV and a relatively long carrier diffusion length [25,26]. That makes SBI materials more favorable to serve as light-harvesting layers than double perovskite [27]. A micrometer-scaled grain of SBI materials, AgBiI_4 and Ag_2BiI_5 , can be obtained using the dynamic hot casting deposition method (DHC). The large grain size of SBI with pinhole-free morphology from DHC confers them to perform a long carrier lifetime. That helps carriers diffuse in an effective path with minor recombination and achieves a PCE of 2.62% [28]. By manipulating the stoichiometric ratio of silver and bismuth, a series of SBI including AgBiI_4 , Ag_2BiI_5 , Ag_3BiI_6 , and AgBi_2I_7 holding direct bandgaps from 1.79 to 1.83 eV were demonstrated. The device composed of Ag_3BiI_6 light absorber layer showed the highest PCE of 4.3% among them [25]. In addition, the co-evaporate deposition with stoichiometric control of AgI and BiI_3 also successfully obtained a series of SBI including AgBiI_4 , AgBi_2I_7 , and Ag_2BiI_5 with bandgaps of 1.80, 1.83, and 1.90 eV [29]. Inheriting the low formation energy of OMHPs, the desired SBI materials can also be manipulated by the stoichiometric ratio of reactants.

Generally, high quality of OMHPs or their derivatives, herein are SBI materials, are prepared by spin-coating method with anti-solvent assisted crystallization. The fine-controlled crystallization step helps to obtain superior film quality in small area devices. Taking advantage of the low formation energy and high defect tolerance of SBI, the large-scalable deposition technique of doctor-blade coating characterized by a low-cost and effective materials-usage technique is considered as another suitable processing for large-area OMHPs or SBI materials [30,31]. Using thermal energy as the driving force can control the solvent removal rate and be conducive to the crystallization and growth of

large grains/domains. Also, the confinement of reactants at substrates allows the precursors of AgI and BiI_3 to transform into the desired product by manipulating the ratio of reactants. Moreover, the spin-orbit coupling effect of lead-free perovskite or their derivatives composed of a relatively light element compared to lead in lead-based perovskite materials exhibits a relatively short carrier lifetime [32,33]. Therefore, providing effective carrier transfer routes is of a feasible path to promote the photovoltaic performance of such photovoltaic materials.

In this study, we demonstrated a thermal-assisted doctor blade (TADB) coating method to fabricate an air-stable SBI material of Ag_3BiI_6 . To enhance the effective carrier transfer in TADB-coated devices, doping-engineered carrier transporting layers were applied to improve the PCE of TADB-coated devices. The PCE of the champion device can be enhanced from 2.06% to 2.77%. The champion device with an active area of 1.00 cm^2 can also attain 2.03%. Owing to the large grain size and contact angle of the Ag_3BiI_6 light absorber prepared by TADB, the devices with such a light absorber layer have outstanding air stability. The PCE of such devices can maintain 90% of its initial PCE after being stored in air for over 3,000 h.

2. Results and discussion

The as-prepared precursor solution of Ag_3BiI_6 light absorber layers was directly deposited onto the as-prepared fluorine-doped tin oxide (FTO) glass coated with the electron transporting layer (ETL) of the mesoporous TiO_2 layer (*meso-TiO₂*) through TADB. Briefly, a substrate was preheated on a hot plate. The doctor-blade coating was processed with blade speed equal to solvent removal rate (detail see in experimental section). The X-ray diffractometer was used to examine both as-cast film and the films with further thermal treatment at different temperatures to achieve the crystallinity and structure of Ag_3BiI_6 light absorber layers. Fig. 1(a) demonstrates as-cast films and the films from TADB coating with various annealing temperatures (characteristic peaks at 12.7° and 29.2° refer to plane (003) and (104) from $R\bar{3}m$ phase of Ag_3BiI_6) [34]. Based on Fig. 1(b), the characteristic peaks at 26.5° , 33.7° , and 37.7° from as-deposited films refer to plane (110), (101), and (200) of fluorine-doped tin oxide. In addition, the peak at 25.3° refers to plane (101) of the anatase TiO_2 from a mesoporous electron transporting layer. Owing to the low formation energy of SBI materials, the as-cast Ag_3BiI_6 film without further annealing process exhibits a similar crystal structure to the films from the TADB coated process. The presence of a secondary phase from β -phase or γ -phase AgI (at 22.3° and 23.6°) in Ag_3BiI_6 films may help to induce the delocalization of silver ion in Ag_3BiI_6 lattice [34]. Also, the mobile Ag^+ can increase the selectivity of carriers and reduce accumulation at the light absorber layer and the transporting layer interface [35]. High crystallinity of the light absorber layers is considered as a beneficial factor for light-induced charge carriers to be transported with minor recombination due to fewer defects. To enhance the crystallinity of the Ag_3BiI_6 films, an external driving force in the form of additional heat was subsequently applied after the films were cast. The crystal grain size of Ag_3BiI_6 layers annealed at various temperatures was calculated according to Scherrer's equation below.

$$\tau = \frac{K\lambda}{\beta\cos(\theta)} \quad (1)$$

Where τ is the grain size of the Ag_3BiI_6 crystal, K is a dimensionless geometrical factor, λ is the wavelength of X-ray ($\text{Cu } K_\alpha$ radiation, 1.54 Å), β is the full width at half maximum (FWHM) in radians, and θ is the Bragg's diffraction angle. The calculated grain size (based on the plane (104) at 2θ of 29.2°) was 23.2 nm for as-cast film, and 23.3 nm, 24.3 nm, 34.6 nm, and 35.7 nm for the Ag_3BiI_6 films subsequently annealed at 120, 140, 160, and 180 °C, respectively (as shown in Fig. 1(c)). Although the high crystallinity corresponding to low micro-defects from grain boundaries in Ag_3BiI_6 films is conducive to carrier transportation,

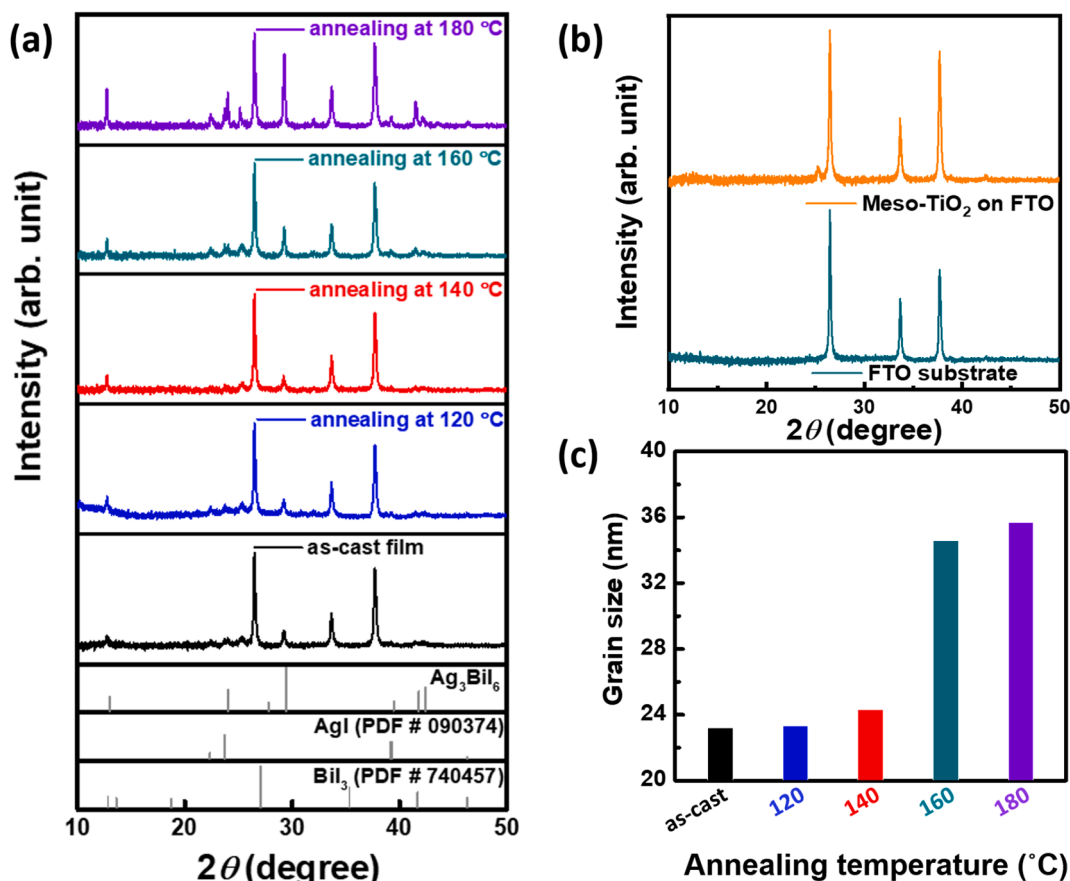


Fig. 1. Crystal structures of various doctor-blade coated silver bismuth iodide layers: (a) prepared at various annealing temperatures, (b) diffraction patterns of a substrate (FTO) and a substrate deposited with electron transporting layer (FTO/meso-TiO₂), and (c) calculated Ag₃BiI₆ grain size of doctor-blade coated silver bismuth iodide layers prepared at various annealing temperatures.

the rapid grain growth rate during the annealing process possibly induces surface roughness as shown in Fig. S1. In Fig. S1(a), the root-mean-square roughness (R_q) of Ag₃BiI₆ films first decreased with the annealing temperature increased. The Ag₃BiI₆ films annealed at 160 °C exhibited the lowest R_q of 52.7 nm in the series. An inflected roughness occurred at an annealing temperature of 180 °C. The rapid growth rate not only influenced on the surface roughness but also on the morphology of the films as shown in Fig. S1(b). The rapid grain growth obviously induced grain aggregation with relatively large surface roughness. That adversely influences the stacking of the above layers and leads to macro-scaled defects between layers. Therefore, investigating the photovoltaic performance of devices with such Ag₃BiI₆ films is an effective method to realize the film quality of the light absorber layer and the stacking quality of devices.

In terms of TADB coating, four factors, including precursor concentration, blade gap, annealing temperature, and annealing time, play influential roles to film thickness and crystallinity of Ag₃BiI₆ films. Generally, the thicker the film is, the more incident light can be absorbed by the light absorber layer. Yet, the film thickness also affects the carrier diffusion as incident light with enough energy strikes on Ag₃BiI₆ light absorber layers. The diffusion lengths of electrons and holes are a threshold for effective carrier transportation. Once the film thickness is thicker than carrier diffusion length, the non-radiative recombination occurs and eliminates the charged carriers in light absorber layers. Therefore, counterbalancing film thickness of the light absorber layers helps to effectively harvest incident light and transfer light-excited carriers toward transporting layers with minor non-radiative recombination loss. Furthermore, owing to fewer defects in the crystallinity of the active layer, the charged carriers can fluently migrate in this active

layer.

To investigate the correlation between the above factors and photovoltaic performance, devices from various processing conditions were prepared to show how they impact the output of finalized efficiency. To reach the trade-off between incident light harvesting and carrier transferring, optimizing film thickness by manipulating the precursor concentration and processing blade gap is a straightforward method to achieve this goal. The corresponding film thickness of Ag₃BiI₆ light absorber layers processed at different conditions, blade gap and precursor concentration, were measured by atomic force microscopy (AFM). The results were shown in Fig. S2 and the statistic film thickness was also shown in Fig. S3. The film thickness of Ag₃BiI₆ light absorber layers was obviously enlarged by the increasing blade gap and precursor concentration. As shown in Fig. 2(a) and (b), the device performance climbed to the highest value at a concentration of 0.30 M and a blade gap of 300 μm, whose thickness was around 170 nm. That implies the obtained films exhibit the optimized film thickness and demonstrate the highest PCE. Also, annealing temperature and duration of processing conditions determine the surface morphology and crystallinity of films. To compare the quality of obtained active layers, the PCE of the device with Ag₃BiI₆ light absorber layers is shown in Fig. 2(c) and (d). The devices with Ag₃BiI₆ light absorber layers annealed at 160 °C for 7 min exhibit the highest PCE compared to those prepared in other conditions. As a result, for all further discussion, TADB for the Ag₃BiI₆ light absorber layer followed these conditions, where the concentration of the precursor was 0.3 M, the blade gap for processing was 300 μm, and the annealing process was at 160 °C for 7 min to obtain the film thickness around 170 nm.

After optimizing the TADB-coated Ag₃BiI₆ light absorber layer, we

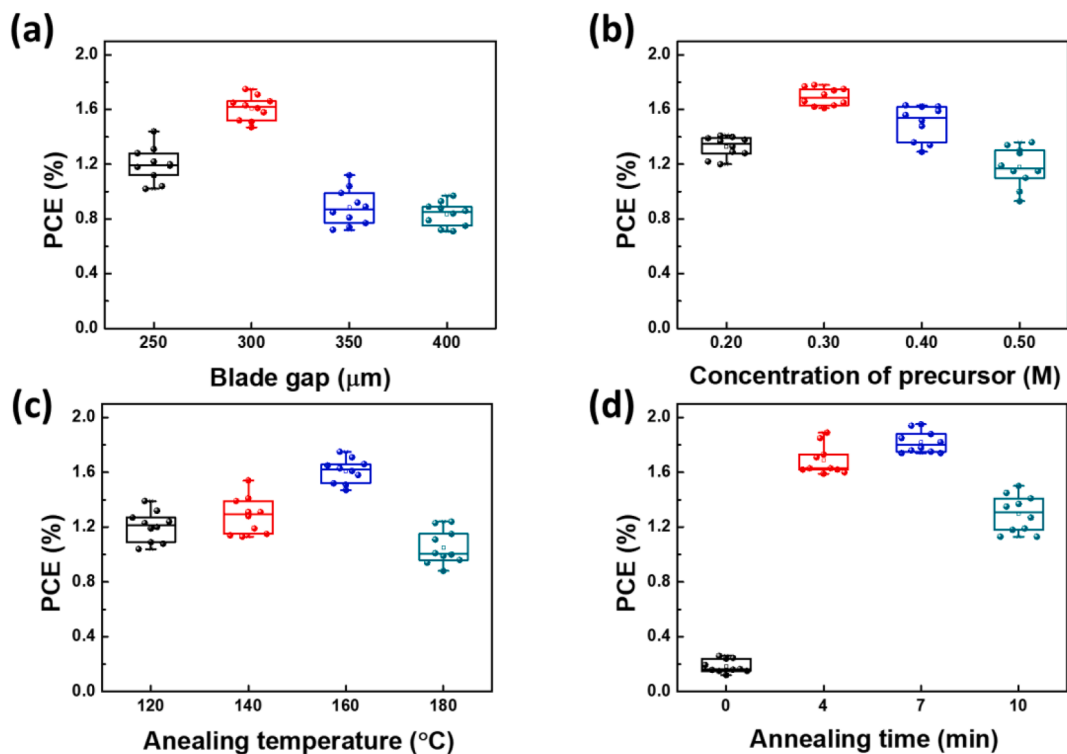


Fig. 2. Correlation between processing parameter of Ag_3BiI_6 light absorber layers and their photovoltaic performance of device: (a) blade gap, (b) precursor concentration, (c) annealing temperature, and (d) annealing time.

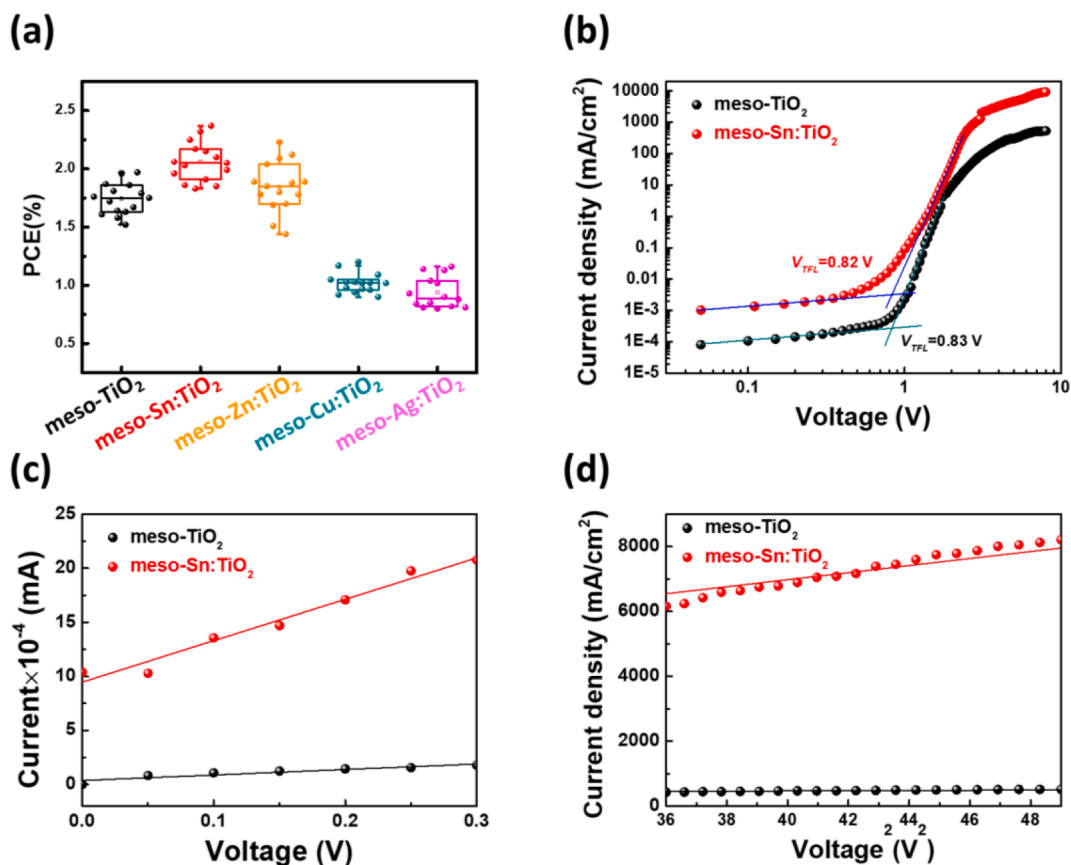


Fig. 3. Photovoltaic performance of devices with meso-TiO_2 and $\text{meso-metal-doped TiO}_2$ electron transporting layers: (a) PCE distribution of devices with various electron transporting layers. Characterization of electron-only devices with meso-TiO_2 and meso-Sn:TiO_2 electron transporting layer: (b) $J-V$ curves for the SCLC model fitting, (c) $I-V$ curves of the Ohmic region ($I \propto V$), and (d) $J-V^2$ curves of the Child's region ($J \propto V^2$).

focused on the compatibility between the transporting layers and the Ag_3BiI_6 light absorber layer. Note that the transportation of charge carriers, negatively charged electrons and positively charged holes, is directly proportional to the obtained current density. The compatibility between a light absorber layer and transporting layers should be carefully considered to obtain an astute photovoltaic performance that can perform the photoelectronic properties of an Ag_3BiI_6 light absorber layer. Doping engineering is widely used to enhance the conductivity of semiconducting materials by increasing the carrier density. As a result, we first aimed to focus on the ETLs in the devices. As the first deposited layer to construct a device, ETLs influence on deposited light absorber layers. A series of metals, including tin, zinc, silver, and copper, were selected as dopants to improve the conductivity and energy alignment between ETLs and Ag_3BiI_6 layers. The preliminary tests for metal doped meso-TiO_2 were first fixed at 1.0 mol%. The PCE distribution from the devices whose light absorber layers deposited onto pristine or various metal-doped meso-TiO_2 electron transporting layers were shown in Fig. 3(a). Among them, meso-Sn:TiO_2 ETL devices show superior PCE to the others. The J - V curves of champion devices with various ETL are shown in Fig. S4(a). The low concentration of Sn dopant might be insufficient to enhance the conductivity of ETL. Whereas the high concentration condition, the excessed Sn dopant might cause an impurity scattering effect and inhibit carrier transporting in the meso-Sn:TiO_2 . As a result, a series of the doping concentration of Sn into meso-TiO_2 were further conducted to optimize the doping concentration. Based on the results in Fig. S4(b), the optimized concentration of meso-Sn:TiO_2 was 1.0 mol%.

To better understand the difference between pristine and meso-Sn:TiO_2 , the J - V curve of electron-only devices, composed of FTO/compact $\text{TiO}_2/\text{meso-TiO}_2$ or $\text{meso-Sn:TiO}_2/\text{Au}$, was examined by fitting the space charge limited current model (SCLC model). For the SCLC model, it can be categorized into three regions: the Ohmic region ($I \propto V$), the space charge limited current region (SCLC region, $I \propto V^n$, $n > 2$), and the Child's region ($I \propto V^{3/2}$). Each region reveals corresponding information about the constructed pristine meso-TiO_2 or meso-Sn:TiO_2 ETL. The transient point (trap filled voltage, V_{TFL}) between the Ohmic and the SCLC regions indicates the trap density of subjected materials. The V_{TFL} is proportional to trap density in a material. Fig. 3(b) shows that the V_{TFL} from meso-TiO_2 and meso-Sn:TiO_2 ETL were hardly different. That implies the improvement of PCE from devices with meso-Sn:TiO_2 ETL can be ascribed to the advancement of conductivity rather than the reduction of trap density. When focusing on the linear region of the Ohmic region ($I \propto V$) in Fig. 3(c), the current was highly related to the conductivity of ETL following the empirical equation below:

$$I = \sigma_0 \frac{A}{d} V \quad (2)$$

Where A is the active area, d is the film thickness, and σ_0 is the conductivity of the film. The calculated conductivity of the meso-Sn:TiO_2 ETL was $9.55 \text{ mS}\cdot\text{cm}^{-1}$, compared to $1.28 \text{ mS}\cdot\text{cm}^{-1}$ for the pristine meso-TiO_2 ETL. The mobility can also be derived from the Child's region, as shown in Fig. 3(d) through the Mott-Gurney law:

$$J = \frac{9}{8} \epsilon \epsilon_0 \frac{V^2}{d^3} \quad (3)$$

Where ϵ is the dielectric constant, ϵ_0 is the permittivity of free space in a vacuum of TiO_2 , and d is the thickness of meso-TiO_2 or meso-Sn:TiO_2 . The calculated electron mobility for the meso-TiO_2 ETL was $1.55 \times 10^5 \text{ cm}^2 \cdot \text{V} \cdot \text{s}^{-1}$, compared to $5.30 \times 10^4 \text{ cm}^2 \cdot \text{V} \cdot \text{s}^{-1}$ for the meso-Sn:TiO_2 ETL, inferring that the conductivity enhancement of Sn-doped ETL effectively promoted the carriers transport in ETL and rationally increased the photocurrent as well as PCE of devices.

On the other hand, the compatibility of the hole transporting layers (HTL) for Ag_3BiI_6 light absorber layers is another factor determining a carrier transportation capability in a device. Fig. S5 shows a preliminary test for various HTLs. Although the PCE of the device with PTAA as HTL

stood out from the others, the mediocre PCE is necessary to be improved. The low current density of the device composed of pristine PTAA can be attributed to the relatively low intrinsic carrier density of pristine PTAA. Incorporating an organic salt as a p-type dopant is a feasible method to enhance the carrier density of PTAA. Therefore, a small amount (from 1 μmol to 8 μmol) of lithium bis(trifluoromethanesulfonyl)imide (Li-TFSI) additive was incorporated into PTAA to induce the oxidation phase of PTAA^+ or charge-transfer complex [36,37]. That has been reported to facilitate the charge-transfer process due to the improvement of PTAA conductivity [38]. Fig. 4 demonstrates the doping effect of Li-TFSI in PTAA. Fig. 4(a) shows that 2 μmol of Li-TFSI additive showed superior photovoltaic performance to the others. The J - V curves and external quantum efficiencies (EQE) in Fig. 4(b) and (c) of the champion devices pointed out that the progress mainly came from the enhancement of current density. The sharp peak at short wavelength in EQE spectrum can be ascribed to high absorption at 420 nm from the trivial amount of residual AgI whose energy bandgap is located at around 3 eV in Ag_3BiI_6 films [28].

In addition to the conductivity of carrier transporting layers, band alignment in a photovoltaic device plays an influential role in both carrier separation and built-in potential (E_{bi}) in a device. An E_{bi} in a device is a driving force that triggers positively charged holes to migrate along with an electric field and negatively charged electrons to migrate in the opposite direction. Therefore, the appropriate energy alignment between layers facilitates electron-hole pairs separation. To investigate whether doping transporting layers affects E_{bi} in devices, the energy level of each layer was examined using an ultraviolet photoelectron spectrometer (UPS). Fig. 5(a)-(c) demonstrate the band structure of each layer in devices, and Fig. 5(d) summarizes the band diagram of devices with pristine or modified transporting layers. Based on a previous study, slight doping of an appropriate dopant in TiO_2 can shift conduction band minimum (CBM) upward to a shallow energy level [39]. The energy level diagram of pristine meso-TiO_2 and meso-Sn:TiO_2 ETL was calculated from UPS (Fig. 5(a)) and UV-vis spectra (Fig. S6). The valance band maximum (VBM) and CBM were -7.85 eV and -4.09 eV for the pristine meso-TiO_2 ETL and -7.59 eV and -3.86 eV for the meso-Sn:TiO_2 ETL. The results indicated that doping Sn into meso-TiO_2 could shift the VBM and CBM to a higher energy level. The VBM and CBM for the Ag_3BiI_6 light absorber layer were calculated to be -5.49 eV and -3.59 eV , as shown in Fig. 5(b). Thus, the suitable band alignment could facilitate the electron injection from the Ag_3BiI_6 light absorber layer to the meso-Sn:TiO_2 ETL. For hole transporting, the VBM and CBM for HTL were determined to be -5.41 eV and -2.41 eV for the pristine PTAA and -5.33 eV and -2.33 eV for the 2 μmol Li-TFSI doped PTAA (Fig. 5(c)). The well-aligned energy level of devices with modified transporting layers can facilitate the separation of the electron-hole pairs and harvest a higher photocurrent than those with inferior electron-hole pair separations. The band diagram of devices with the pristine and the modified transporting layers was summarized in Fig. 5(d).

In addition to the smooth transfer path of charge carriers, doping transporting layers can enlarge the quasi-Fermi level splitting (QFLS) between ETL/ Ag_3BiI_6 and $\text{Ag}_3\text{BiI}_6/\text{HTL}$ interfaces. QFLS between both interfaces has been reported to be ideally equal to V_{OC} acquired from a photovoltaic. All energy levels, including quasi-fermi levels (E_{fe} and E_{fh}) were depicted, and all the scenarios were demonstrated in Fig. S7(a). Although a slight decrease of V_{OC} occurred in devices with Li-TFSI doped PTAA as an HTL, the enhanced conductivity of HTL promoted the photocurrent of devices. As a result, the device with modified TLs still demonstrated the highest photovoltaic performance after it counterbalanced the decreased V_{OC} by enhanced J_{SC} as shown in Fig. S7(b). The J - V curves of the champion device with and without transporting layers are shown in Fig. 6(a). Owing to both energy alignment and conductivity progress, the V_{OC} enhanced from 0.62 V to 0.70 V, and the J_{SC} increased from $5.56 \text{ mA}/\text{cm}^2$ to $6.44 \text{ mA}/\text{cm}^2$. The corresponding PCE from the champion device can achieve 2.77%. To evaluate the hysteresis phenomena in the device with modified transporting layers, the hysteresis

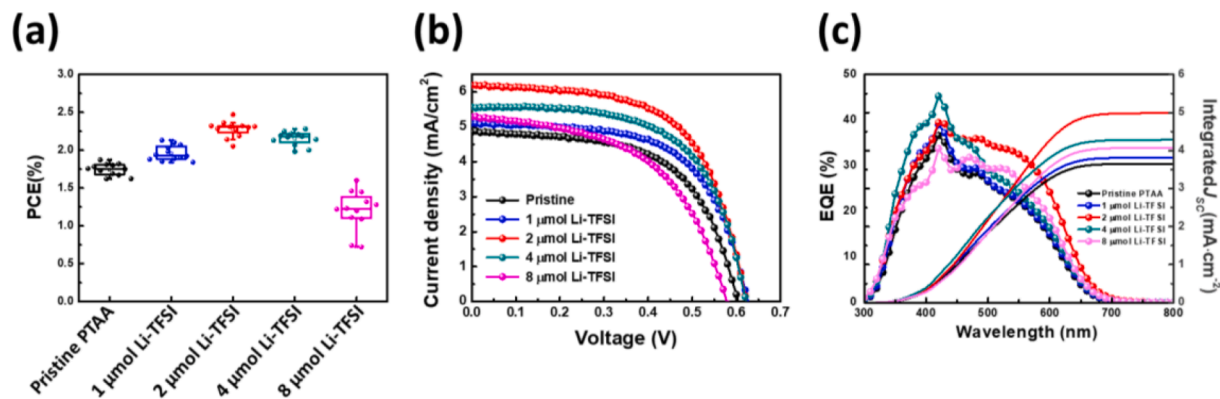


Fig. 4. Photovoltaic performance of devices with Li salt doped PTAA hole transporting layer: (a) PCE distribution, (b) J - V curves of the champion devices, and (c) external quantum efficiencies of devices with various concentrations of Li-doped PTAA HTL.

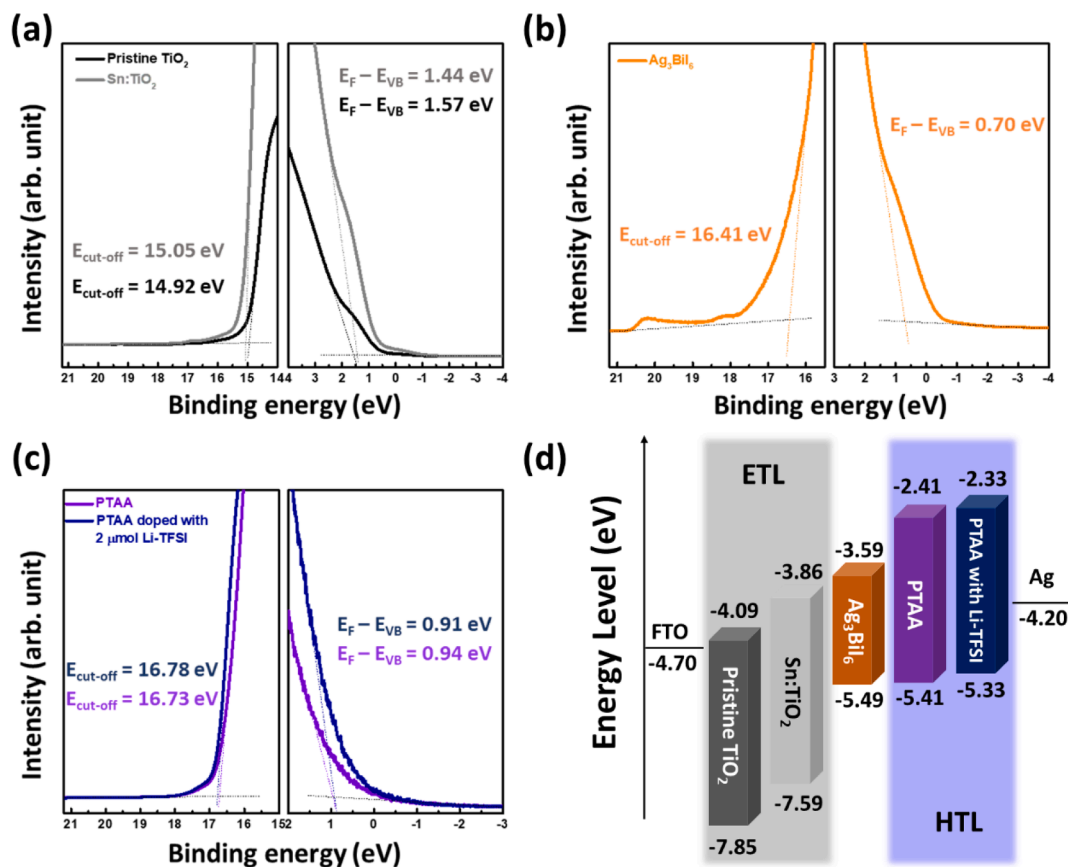


Fig. 5. Band structure analysis of each layer in the photovoltaic device using ultraviolet photoelectron spectroscopy: (a) pristine *meso*-TiO₂ and *meso*-Sn:TiO₂ electron transporting layers, (b) Ag₃BiI₆, (c) PTAA and Li-TFSI doped PTAA hole transporting layers, and (d) the band diagram of an entire device.

index (HI) was calculated as followed the Eq. (4) to examine the hysteresis effect in such devices. The lower the HI value, the weaker the hysteresis in a measured device. The calculated HI was 0.036 for the device without modified TLs and 0.019 for the device with modified TLs. Although both HI values from the devices were trivial with the mesoporous ETLs, the minor HI value was still obtained in the device with modified TLs compared to it in the device without modified TLs. That manifested that modified TLs can effectively facilitate carrier transfer at interfaces or mobility in TLs and provide an effective path for charge carriers transfer from Ag₃BiI₆ light absorber layers to both side of TLs.

$$HI = \frac{J_{RS}(0.8V_{OC}) - J_{FS}(0.8V_{OC})}{J_{RS}(0.8V_{OC})} \quad (4)$$

To determine the light response of incident light at various wavelengths, the light-induced constant potential difference (CPD) of the absorber layer was shown in Fig. 6(b). The light absorber layer's CPD infers the light response of the Ag₃BiI₆ light absorber layer as incident light strikes. Typically, the incident light with greater energy than the energy bandgap of the light absorber layer causes a thermalization loss. In contrast, when the energy of incident light is lower than the energy bandgap of an absorber layer, it leads to transmission loss. As a result, the incident light exhibiting the same energy as the bandgap of a light absorber layer can be the most effectively used with minor energy loss. Consistent with the energy bandgap of Ag₃BiI₆ materials, as shown in Fig. S6(b), the highest CPD occurred when the absorber layer was irradiated with a 650 nm light.

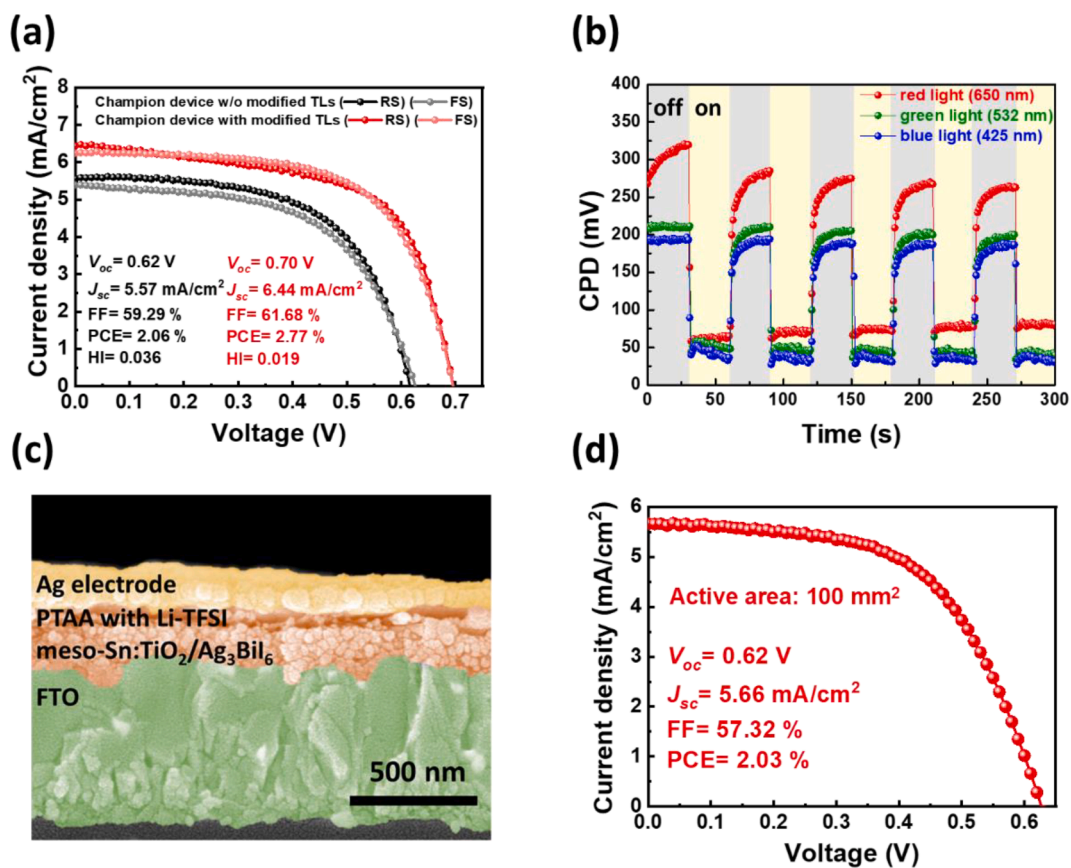


Fig. 6. Photovoltaic performance of the champion device: (a) J - V curve from champion devices with a 4.0 mm² active area, (b) light-induced constant potential difference of the champion device under various light sources, (c) cross-sectional FE-SEM image for the champion device, and (d) J - V curve of the champion device with an active area of 100.0 mm².

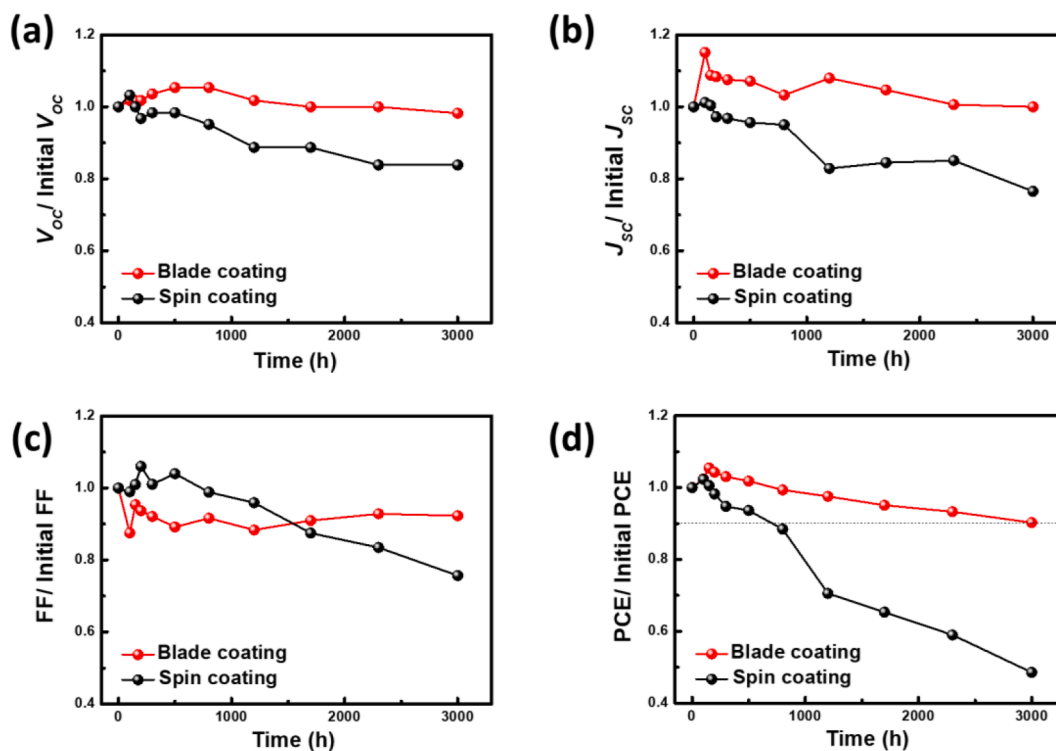


Fig. 7. Performance tracing of unencapsulated Ag₃BiI₆ devices in ambient air: (a) V_{oc} , (b) J_{sc} , (c) fill factor, and (d) PCE.

To show the architecture of the device, a cross-sectional image acquired from field-emission scanning electron microscopy (FE-SEM) was used to observe the thickness of each layer in the device, as shown in Fig. 6(c). Due to the inferior carrier diffusion length of the Ag_3BiI_6 light absorber layer to conventional lead-based perovskite materials, the film was thinner (as shown in Fig. S3 of around 170 nm) than conventional lead-based perovskite material, which can be over half a micrometer. The J - V curve of a one hundred square millimeter champion device with optimized Ag_3BiI_6 and transporting layers is shown in Fig. 6(d), and its PCE achieved 2.03%. The corresponding photography of devices with the different active area are shown in Fig. S8.

Moreover, the long-term stability of photovoltaic performance is also a crucial characteristic for evaluating the reliability of devices. Light instability is one of the concerns for lead-based perovskite photovoltaics owing to their ionic nature. The migration of A-site cation in lead-based perovskite materials might induce instability as they are continuously struck by light. Fig. S9 demonstrated the continuous J - T curve of the Ag_3BiI_6 device with modified TLs. The applied voltage based on V_{max} in the J - V curve (Fig. S9(a)) was set at 0.51 V to acquire photocurrent and PCE. Both PCE and photocurrent can maintain over 90% of their initial value as shown in Fig. S9(b). That implied such a photovoltaic exhibited relatively stable power output under a continuous operating condition. Fig. 7 shows the tracing photovoltaic performance of unencapsulated devices in an ambient environment, prepared by the spin coating method or the TADB method. The device prepared by TADB maintained 90% of its initial PCE after 3,000 h of storage in such conditions. On the other hand, the spin-coated device only held \sim 50% of its initial PCE after storing in the same condition for 3,000 h. The main deterioration of PCE came from the decrease of photocurrent and fill factor, which were lower than 90% of their initial value. Fig. S10 shows the morphological difference of the Ag_3BiI_6 light absorber layers from spin-coating or TADB deposition. The domain sizes of spin-coated Ag_3BiI_6 (Fig. S10(a-1)) were much smaller than that in the film from TADB deposition (Fig. S10(a-2)). That can be attributed to the rapid nucleation site formation as dripping anti-solvent to assist crystallization during the spin-coating process. Although the surface morphology of the spin-coated film was relatively smooth (Fig. S10(b-1), $R_q = 37.5$ nm), the small domain sizes resulted in more significant numbers of boundaries than that of the TADB coated film (Fig. S10(b-2), $R_q = 51.4$ nm). The morphological differences, namely domain size, roughness, and the number of boundaries led to different contact angles of the films as shown in Fig. S10(c-1) and (c-2). The larger contact angle can decelerate the moisture infiltration as the devices were subjected to a humid surrounding. Therefore, the sharp decrease of the photocurrent and fill factor of the spin-coated device can be rationally ascribed to the morphological difference. The large domain size with a relatively low density of boundaries and large contact angle of TADB coated films can inhibit the adsorption of gas molecules, especially oxygen molecules and moisture, at/in the active layer. The adsorbed gas molecules might trap the charge carrier to reach a low free energy condition [42,43]. It infers that the fewer the gas molecules adsorbed at the active layer, the more stable the photovoltaic performance expected for the long-term stability test. Therefore, the device with a light absorber layer of Ag_3BiI_6 from TADB demonstrates much longer stability under the interface of oxygen and moisture in an ambient environment than the spin-coated device.

3. Conclusion

In this study, we successfully fabricated a rudorffite of Ag_3BiI_6 solar cell through the thermal-assisted doctor blade coating method. By applying dopants into carrier transporting layers and monitoring the crystallization condition of the light absorber layer of Ag_3BiI_6 , the PCE of champion rudorffite solar cells can be improved from 2.06% to 2.77%. A large one hundred square millimeter device was fabricated using the thermal-assisted doctor blade coating. It demonstrated a PCE of 2.03%. The well-aligned energy level of the modified transporting

layers confers carrier transfer to process with minor barriers and accumulation between interfaces. That is beneficial to the long-term stability of modified Ag_3BiI_6 solar cells. The PCE of a modified Ag_3BiI_6 solar cell can maintain 90% of its initial PCE after 3,000 h of storage without encapsulation in an ambient environment. This study gives clear information for lead-free rudorffite materials as an active layer toward realizing eco-friendly photovoltaics.

4. Experimental section

4.1. Material and method

In this study, silver iodide (Alfa Aesar, $\geq 99.9\%$), bismuth iodide (Alfa Aesar, $\geq 99.9\%$), titanium isopropoxide (Acros, 99.99%), titanium diisopropoxide bis(acetylacetonate) (Sigma-Aldrich, 75 wt% in isopropanol), bis(trifluoromethane)sulfonimide lithium salt (Sigma-Aldrich, 99.95%), tin (II) acetate (Sigma-Aldrich, 99.99%), copper(II) acetate (Sigma-Aldrich, 99.99%), silver nitrate (Sigma-Aldrich, 99.99%), zinc nitrate (Sigma-Aldrich, 99.99%), poly(triaryl amine) (Sigma-Aldrich, Mn = 7,000–10,000), poly({4,8-bis[(2-ethylhexyl)oxy]benzo[1,2-b:4,5-b'] dithiophene-2,6-diyl}{3-fluoro-2-[(2-ethylhexyl)carbonyl]thieno[3,4-b] thiophenediyl}).

(PTB7, 1-material), poly(3-hexylthiophene-2,5-diyl) (P3HT, Rieke material, regioregular, Mn = 51,000, $>95\%$), dimethyl sulfoxide (ECHO, $>99.9\%$), chlorobenzene (Acros, 99.8%), toluene (ECHO, $>99.5\%$), 2-propanol (STAREK, $>99.8\%$), α -terpineol ($\text{C}_{10}\text{H}_{18}\text{O}$, Merck, 90%), ethyl cellulose (Acros, ethoxyl content 48%), acetic acid (Arcos, 99.99%) were used without any pre-treatment. The preparation of *meso*- TiO_2 paste followed our previous works [41,44]. Pristine and metal-doped TiO_2 nanocrystal were all prepared using the sol-gel method. After, the products were mixed with α -terpineol and ethyl cellulose to form a 23.0 wt% paste [44]. To prepare the rudorffite precursors, 211.3 mg of silver iodide and 176.9 mg of bismuth iodide were weighed and transferred into a 7.0 mL vial. 1 mL of DMSO was added to the vial to obtain a 0.3 M silver bismuth iodide precursor solution. To prepare hole transporting layer precursors, 15.0 mg of P3HT, PTB7, and PTAA were separately dissolved into 1.0 mL of chlorobenzene. For the modified hole-transporting materials of PTAA, 15.0 mg of PTAA with 8.0 μmol of Li-TFSI additive and pristine PTAA solution were first prepared. The desired concentrations of 1.0 μmol , 2.0 μmol , and 4.0 μmol of Li-TFSI additive in PTAA were prepared by mixing the desired volume of pristine PTAA solution and PTAA with 8.0 μmol of Li-TFSI solution.

4.2. Device fabrication

The device architecture followed the established mesoporous *n-i-p* structure reported elsewhere [41,44,45]. Before the coating process, FTO glasses (7 Ω , FrontMaterials Co. Ltd.) were washed sequentially with deionized water, acetone, and isopropanol to remove adsorbed organic contaminants. A compact TiO_2 layer was deposited onto the conductive side of FTO glass by using spray pyrolysis with titanium diisopropoxide bis(acetylacetonate) solution. The prepared *meso*- TiO_2 paste was screen-printed onto the compact layer of TiO_2 , followed by a half-hour of calcination at 500 $^\circ\text{C}$. After the glasses cooled to room temperature, the as-prepared precursor solution of silver bismuth iodide was deposited on the glass with the thermal-assisted doctor blade coating method. A hot plate was set at 120 $^\circ\text{C}$ for 15 min to reach thermal equilibrium. A constant volume of the precursor was dropped onto the edge of the preheated substrate. The blade gap was set at the desired height, and the moving rate of the doctor-blade was controlled manually. To obtain a smooth film morphology, the moving speed of the doctor-blade was controlled evenly with solvent evaporation rate. For the as-prepared film (control device), the coating process was finished as the doctor-blade moved from the edge to the other edge of a substrate without further annealing steps. In contrast, the target devices were further annealing at the desired temperature for the desired amount of time. For hole

transporting layers deposition, 50.0 μL of an as-prepared precursor of hole-transporting materials, including P3HT, PTB7, and PTAA, were spin-coated (at 3,000 rpm for 30 s) onto the Ag_3BiI_6 light absorber layers. Subsequently, the device was completed after either 0.04 cm^2 or 1 cm^2 of 120-nm thick silver electrode active layers were thermal evaporated onto the hole transporting layer.

4.3. Characterization

Ultraviolet–visible (UV–Vis) absorption spectrum was measured using UV–vis spectrometer (V-730, Jasco). The UPS (Sigma Probe, Thermo VG-Scientific) equipped HeI (21.2 eV) light source was applied to investigate the energy level of the active layers. Constant potential difference (CPD) was acquired from a scanning Kelvin probe analyzer equipped with a 2-mm gold tip (KP Technology, SKP 5050) and 300 mW of red, green, and blue LED light sources. The film morphologies and cross-sectional images of devices were acquired using a Field-Emission Scanning Electron Microscope (FE-SEM) (SU-8010, HITACHI) with an accelerating voltage of 10 kV. The surface topography mappings of Ag_3BiI_6 light absorber layers were collected by AFM (Veeco, MultiMode Atomic Force Microscope) in tapping mode. The J – V curves of the devices were measured with a digital source meter (2400, Keithley) under simulated solar illumination at 100 mW cm^{-2} , AM 1.5G standard, and with a calibrated Si-reference cell (Bunkokeiki, BS-520BK) with a KG-5 filter. The External Quantum Efficiency (EQE) spectra were recorded using an IPCE spectrometer (EQE-R-3011, Enli Technology Co. Ltd). The crystallographic structure analysis was analyzed using an X-ray Diffractometer equipped with cross beam optics (Rikagu, SmartLab, 220C212).

Declaration of Competing Interest

The authors declare that they have no known competing financial interests or personal relationships that could have appeared to influence the work reported in this paper.

Data availability

The authors do not have permission to share data.

Acknowledgments

The authors appreciate Dr. Ming-Tao Lee (BL-13A1), Dr. Jyh-Fu Lee (BL-17C1) and Dr. Ting-Shan Chan (BL-101C1) at National Synchrotron Radiation Research Centre for useful discussion and suggestions, and Miss Y.-M. Chang at Instrumentation Centre of National Tsing Hua University for TEM analysis. The authors also thank the Microscopy Center at Chang Gung University for technical assistance. The financial support from National Science and Technology Council, Taiwan (Project No. 111-2628-E-182-001-MY2, and 111-2221-E-182-040-MY3), Chang Gung University (QZRPD181) and Chang Gung Memorial Hospital at Linkou (CMRPD2M0121 and BMRPC74) are highly appreciated.

Appendix A. Supplementary data

Supplementary data to this article can be found online at <https://doi.org/10.1016/j.cej.2022.138807>.

References

- [1] A. Kojima, K. Teshima, Y. Shirai, T. Miyasaka, Organometal Halide Perovskites as Visible-Light Sensitizers for Photovoltaic Cells, *J. Am. Chem. Soc.* 131 (17) (2009) 6050–6051.
- [2] Y. Gao, M. Zhang, X.u. Zhang, G. Lu, Decreasing Exciton Binding Energy in Two-Dimensional Halide Perovskites by Lead Vacancies, *J. Phys. Chem. Lett.* 10 (14) (2019) 3820–3827.
- [3] F. Zhang, B. Yang, Y. Li, W. Deng, R. He, Extra long electron–hole diffusion lengths in $\text{CH}_3\text{NH}_3\text{Pb}_{1-x}\text{Cl}_x$ perovskite single crystals, *J. Mater. Chem. C* 5 (33) (2017) 8431–8435.
- [4] J. Huang, Y. Yuan, Y. Shao, Y. Yan, Understanding the physical properties of hybrid perovskites for photovoltaic applications, *Nat. Rev. Mater.* 2 (2017) 17042.
- [5] S. De Wolf, J. Holovsky, S.-J. Moon, P. Löper, B. Niesen, M. Ledinsky, F.-J. Haug, J.-H. Yum, C. Ballif, Organometallic Halide Perovskites: Sharp Optical Absorption Edge and Its Relation to Photovoltaic Performance, *J. Phys. Chem. Lett.* 5 (2014) 1035–1039.
- [6] <https://www.nrel.gov/pv/cell-efficiency.html>.
- [7] V.K. Ravi, G.B. Markad, A. Nag, Band Edge Energies and Excitonic Transition Probabilities of Colloidal CsPbX_3 (X = Cl, Br, I) Perovskite Nanocrystals, *ACS Energy Lett.* 1 (4) (2016) 665–671.
- [8] S.-C. Liu, C.-M. Dai, Y. Min, Y. Hou, A.H. Proppe, Y. Zhou, C. Chen, S. Chen, J. Tang, D.-J. Xue, E.H. Sargent, J.-S. Hu, An antibonding valence band maximum enables defect-tolerant and stable GeSe photovoltaics, *Nat. Commun.* 12 (2021) 670.
- [9] Y. Jiang, L. Qiu, E.J. Juarez-Perez, L.K. Ono, Z. Hu, Z. Liu, Z. Wu, L. Meng, Q. Wang, Y. Qi, Reduction of lead leakage from damaged lead halide perovskite solar modules using self-healing polymer-based encapsulation, *Nat. Energy* 4 (7) (2019) 585–593.
- [10] B. Niu, H. Wu, J. Yin, B. Wang, G. Wu, X. Kong, B. Yan, J. Yao, C.-Z. Li, H. Chen, Mitigating the Lead Leakage of High-Performance Perovskite Solar Cells via In Situ Polymerized Networks, *ACS Energy Lett.* 6 (10) (2021) 3443–3449.
- [11] F. Hao, C.C. Stoumpos, D.H. Cao, R.P.H. Chang, M.G. Kanatzidis, Lead-free solid-state organic–inorganic halide perovskite solar cells, *Nat. Photonics* 8 (6) (2014) 489–494.
- [12] L. Lanzetta, T. Webb, N. Zibouche, X. Liang, D. Ding, G. Min, R.J.E. Westbrook, B. Gaggio, T.J. Macdonald, M.S. Islam, S.A. Haque, Degradation mechanism of hybrid tin-based perovskite solar cells and the critical role of tin (IV) iodide, *Nat. Commun.* 12 (2021) 2853.
- [13] J. Pascual, G. Nasti, M.H. Aldamasy, J.A. Smith, M. Flatken, N. Phung, D. Di Girolamo, S.-H. Turren-Cruz, M. Li, A. Dallmann, R. Avolio, A. Abate, Origin of Sn (ii) oxidation in tin halide perovskites, *Mater. Adv.* 1 (2020) 1066–1070.
- [14] T. Mahmoudi, W.-Y. Rho, M. Kohan, Y.H. Im, S. Mathur, Y.-B. Hahn, Suppression of $\text{Sn}^{2+}/\text{Sn}^{4+}$ oxidation in tin-based perovskite solar cells with graphene-tin quantum dots composites in active layer, *Nano Energy* 90 (2021), 106495.
- [15] F. Igbari, Z.-K. Wang, L.-S. Liao, Progress of Lead-Free Halide Double Perovskites, *Adv. Energy Mater.* 9 (2019) 1803150.
- [16] S.M. Jain, T. Edvinsson, J.R. Durrant, Green fabrication of stable lead-free bismuth based perovskite solar cells using a non-toxic solvent, *Commun. Chem.* 2 (2019) 91.
- [17] C. Soykan, H. Gocmez, The physical properties of bismuth replacement in lead halogen perovskite solar cells: $\text{CH}_3\text{NH}_3\text{Pb}_{1-x}\text{Bi}_x\text{I}_3$ compounds by ab-initio calculations, *Results Phys.* 13 (2019), 102278.
- [18] S. Attique, N. Ali, S. Ali, R. Khatoun, N. Li, A. Khesro, S. Rauf, S. Yang, H. Wu, A Potential Checkmate to Lead: Bismuth in Organometal Halide Perovskites, Structure, Properties, and Applications, *Adv. Science* 7 (2020) 1903143.
- [19] J.K. Pious, C. Muthu, S. Dani, A. Saeki, C. Vijayakumar, Bismuth-Based Zero-Dimensional Perovskite-like Materials: Effect of Benzylammonium on Dielectric Confinement and Photoconductivity, *Chem. Mater.* 32 (2020) 2647–2652.
- [20] Z. Jin, Z. Zhang, J. Xiu, H. Song, T. Gatti, Z. He, A critical review on bismuth and antimony halide based perovskites and their derivatives for photovoltaic applications: recent advances and challenges, *J. Mater. Chem. A* 8 (2020) 16166–16188.
- [21] M. Xia, J.-H. Yuan, G. Niu, X. Du, L. Yin, W. Pan, J. Luo, Z. Li, H. Zhao, K.-H. Xue, X. Miao, J. Tang, Unveiling the Structural Descriptor of $\text{A}_3\text{B}_2\text{X}_9$ Perovskite Derivatives toward X-Ray Detectors with Low Detection Limit and High Stability, *Adv. Funct. Mater.* 30 (2020) 1910648.
- [22] Y. Sun, A.J. Fernández-Carrion, Y. Liu, C. Yin, X. Ming, B.-M. Liu, J. Wang, H. Fu, X. Kuang, X. Xing, Bismuth-Based Halide Double Perovskite $\text{Cs}_2\text{LiBiCl}_6$: Crystal Structure, Luminescence, and Stability, *Chem. Mater.* 33 (2021) 5905–5916.
- [23] W. Ning, F. Wang, B. Wu, J. Lu, Z. Yan, X. Liu, Y. Tao, J.-M. Liu, W. Huang, M. Fahlman, L. Hultman, T.C. Sum, F. Gao, Long Electron-Hole Diffusion Length in High-Quality Lead-Free Double Perovskite Films, *Adv. Mater.* 30 (2018) 1706246.
- [24] C. Wu, Q. Zhang, Y. Liu, W. Luo, X. Guo, Z. Huang, H. Ting, W. Sun, X. Zhong, S. Wei, S. Wang, Z. Chen, L. Xiao, The Dawn of Lead-Free Perovskite Solar Cell: Highly Stable Double Perovskite Cs_2AgBiBr 6 Film, *Adv. Sci.* 5 (2018) 1700759.
- [25] I. Turkevych, S. Kazaoui, E. Ito, T. Urano, K. Yamada, H. Tomiyasu, H. Yamagishi, M. Kondo, S. Aramaki, Photovoltaic Rudorffites: Lead-Free Silver Bismuth Halides Alternative to Hybrid Lead Halide Perovskites, *ChemSusChem* 10 (2017) 3754–3759.
- [26] H. Zhu, A. Erbing, H. Wu, G.J. Man, S. Mukherjee, C. Kamal, M.B. Johansson, H. Rensmo, M. Odellius, E.M.J. Johansson, Tuning the Bandgap in Silver Bismuth Iodide Materials by Partly Substituting Bismuth with Antimony for Improved Solar Cell Performance, *ACS Appl. Energy Mater.* 3 (8) (2020) 7372–7382.
- [27] S. Hosseini, M. Adelifard, The Impact of Cesium and Antimony Alloying on the Photovoltaic Properties of Silver Bismuth Iodide Compounds, *Physica Status Solidi (a)* 218 (2021) 2000774.
- [28] B. Ghosh, B. Wu, X. Guo, P.C. Harikesh, R.A. John, T. Baikie, A.T.S. Aramell, C. Wee, T.C. Guet, S. Sum, N.M. Mhaisalkar, Superior Performance of Silver Bismuth Iodide Photovoltaics Fabricated via Dynamic Hot-Casting Method under Ambient Conditions, *Adv. Energy Mater.* 8 (2018) 1802051.
- [29] M. Khazaei, K. Sardashti, C.-C. Chung, J.-P. Sun, H. Zhou, E. Bergmann, W. A. Dunlap-Shohl, Q. Han, I.G. Hill, J. Jones, D.C. Lupascu, D.B. Mitzi, Dual-source

- evaporation of silver bismuth iodide films for planar junction solar cells, *J. Mater. Chem. A* 7 (5) (2019) 2095–2105.
- [30] K.-M. Lee, S.-H. Chan, M.-Y. Hou, W.-C. Chu, S.-H. Chen, S.-M. Yu, M.-C. Wu, Enhanced efficiency and stability of quasi-2D/3D perovskite solar cells by thermal assisted blade coating method, *Chem. Eng. J.* 405 (2021), 126992.
- [31] K.-M. Lee, W.-H. Chiu, Y.-H. Tsai, C.-S. Wang, Y.-T. Tao, Y.-D. Lin, High-performance perovskite solar cells based on dopant-free hole-transporting material fabricated by a thermal-assisted blade-coating method with efficiency exceeding 21%, *Chem. Eng. J.* 427 (2022), 131609.
- [32] J. Zhang, T. Wu, J. Duan, M. Ahmadi, F. Jiang, Y. Zhou, B. Hu, Exploring spin-orbital coupling effects on photovoltaic actions in Sn and Pb based perovskite solar cells, *Nano Energy* 38 (2017) 297–303.
- [33] W. Li, L. Zhou, O.V. Prezhdo, A.V. Akimov, Spin-Orbit Interactions Greatly Accelerate Nonradiative Dynamics in Lead Halide Perovskites, *ACS Energy Lett.* 3 (9) (2018) 2159–2166.
- [34] A. Crovetto, A. Hajjifarassat, O. Hansen, B. Seger, I.B. Chorkendorff, P.C. K. Vesborg, Parallel Evaluation of the BiI₃, BiOI, and Ag₃BiI₆ Layered Photoabsorbers, *Chem. Mater.* 32 (8) (2020) 3385–3395.
- [35] W. Tress, J.P. Correa Baena, M. Saliba, A. Abate, M. Graetzel, Inverted Current-Voltage Hysteresis in Mixed Perovskite Solar Cells: Polarization, Energy Barriers, and Defect Recombination, *Adv. Energy Mater.* 6 (2016) 1600396.
- [36] J.W. Sun, J.-H. Lee, C.-K. Moon, K.-H. Kim, H. Shin, J.-J. Kim, A Fluorescent Organic Light-Emitting Diode with 30% External Quantum Efficiency, *Adv. Mater.* 26 (32) (2014) 5684–5688.
- [37] H. Méndez, G. Heimel, A. Opitz, K. Sauer, P. Barkowski, M. Oehzelt, J. Soeda, T. Okamoto, J. Takeya, J.-B. Arlin, J.-Y. Balandier, Y. Geerts, N. Koch, I. Salzman, Doping of Organic Semiconductors: Impact of Dopant Strength and Electronic Coupling, *Angew. Chem. Int. Ed.* 52 (30) (2013) 7751–7755.
- [38] F.M. Rombach, S.A. Haque, T.J. Macdonald, Lessons learned from spiro-OMeTAD and PTAA in perovskite solar cells, *Energy Environ. Sci.* 14 (10) (2021) 5161–5190.
- [39] Y.-H. Liao, Y.-H. Chang, T.-H. Lin, S.-H. Chan, K.-M. Lee, K.-H. Hsu, J.-F. Hsu, M.-C. Wu, Boosting the power conversion efficiency of perovskite solar cells based on Sn doped TiO₂ electron extraction layer via modification the TiO₂ phase junction, *Sol. Energy* 205 (2020) 390–398.
- [41] M.-C. Wu, S.-H. Chan, K.-M. Lee, S.-H. Chen, M.-H. Jao, Y.-F. Chen, W.-F. Su, Enhancing the efficiency of perovskite solar cells using mesoscopic zinc-doped TiO₂ as the electron extraction layer through band alignment, *J. Mater. Chem. A* 6 (35) (2018) 16920–16931.
- [42] N. Aristidou, C. Eames, I. Sanchez-Molina, X. Bu, J. Kosco, M.S. Islam, S.A. Haque, Fast oxygen diffusion and iodide defects mediate oxygen-induced degradation of perovskite solar cells, *Nat. Commun.* 8 (2017) 15218.
- [43] K.-C. Hsiao, M.-H. Jao, K.-Y. Tian, T.-H. Lin, D.-P. Tran, H.-C. Liao, C.-H. Hou, J.-J. Shyue, M.-C. Wu, W.-F. Su, Acetamidinium Cation to Confer Ion Immobilization and Structure Stabilization of Organometal Halide Perovskite Toward Long Life and High-Efficiency p-i-n Planar Solar Cell via Air-Processable Method, *Sol. RRL* 4 (2020) 2000197.
- [44] S.-H. Chen, S.-H. Chan, Y.-T. Lin, M.-C. Wu, Enhanced power conversion efficiency of perovskite solar cells based on mesoscopic Ag-doped TiO₂ electron transport layer, *Appl. Surf. Sci.* 469 (2019) 18–26.
- [45] M.-C. Wu, Y.-Y. Li, S.-H. Chan, K.-M. Lee, W.-F. Su, Polymer Additives for Morphology Control in High-Performance Lead-Reduced Perovskite Solar Cells, *Sol. RRL* 4 (2020) 2070063.